TASK QUARTERLY 9 No 1, 37–52

CALCULATION OF VISCOUS INCOMPRESSIBLE FLOW AROUND AN AEROFOIL USING A MODIFIED VELOCITY CORRECTION METHOD

ZBIGNIEW KOSMA

Institute of Applied Mechanics,
Radom University of Technology,
Krasickiego 54, 26-600 Radom, Poland
zkosma@pr.radom.pl

(Received 3 October 2003; revised manuscript received 29 July 2004)

Abstract: The two-dimensional unsteady motion of viscous incompressible fluid around an aerofoil at a large angle of attack has been computed. A modified velocity correction method splitting the velocity field has been designed to solve this problem. First, a tentative velocity field is determined from the equations of momentum conservation for explicit gradients of computational pressure. Then, the Neumann problem for the Poisson equation is solved to estimate the computational pressure, and velocity components are corrected. Test calculations have been made for the case of flow around the NACA 0012 aerofoil with an incidence of 34°. The domain outside the aerofoil was transformed into a canonical one using conformal mapping. Computations were made on 100×100 and 100×200 grids for Reynolds numbers of $\mathrm{Re} = 400$, 600 and 1000. Comparison with numerical and experimental data reported in the literature has shown that the method is suitable for simulating 2-D external viscous flows.

Keywords: Navier-Stokes equation, incompressible viscous flows, velocity correction method, flows over aerofoils

1. The problem

The problem consists in determination of an unsteady external viscous flow around the NACA 0012 aerofoil with an incidence of 34° (Figure 1). Co-ordinates of points specifying the NACA 0012 profile in a normalized system $[-0.5, 0.5]$, in which the chord is assumed to be the unit of length, are given in [1].

The governing equations that describe unsteady incompressible flow of viscous incompressible fluid are the continuity and Navier-Stokes equations. In two dimen-

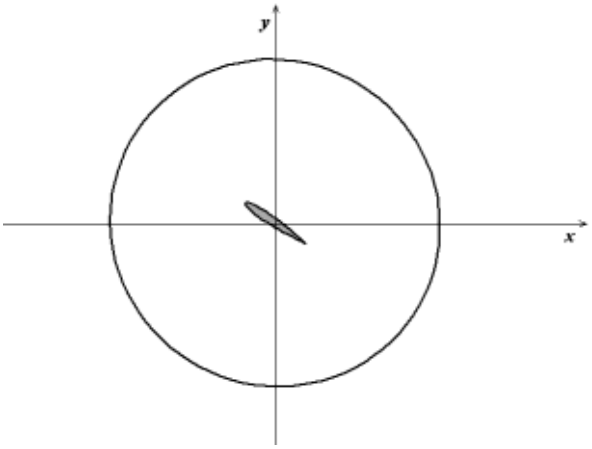

Figure 1. Definition of the computational domain

sions, these equations can be written in the dimensionless form without external forces as [2–4]:

$$\frac{\partial u}{\partial x}+\frac{\partial v}{\partial y}=0, \tag{1}$$

$$\begin{aligned}\frac{\partial u}{\partial t}+\frac{\partial u^2}{\partial x}+\frac{\partial}{\partial y}(uv)&=-\frac{\partial p}{\partial x}+\frac{1}{\mathrm{Re}}\vec{\nabla}^2 u,\\ \frac{\partial v}{\partial t}+\frac{\partial}{\partial x}(uv)+\frac{\partial v^2}{\partial y}&=-\frac{\partial p}{\partial y}+\frac{1}{\mathrm{Re}}\vec{\nabla}^2 v,\end{aligned} \tag{2}$$

where u, v are the velocity components, p is pressure, Re is the Reynolds number, and $\vec{\nabla}^2$ is the Laplace operator.

The velocity components vanish at the profile surface. At an outer boundary the velocity components are assumed to be equal to their values that correspond to potential flow, and the values of pressure can be calculated from the Bernoulli equation.

2. Modified velocity correction method

Velocity correction (splitting, projection, decomposition, Chorin's) methods have recently attracted considerable attention in the area of viscous incompressible flow calculations (see for example [5–36]). These methods have gained popularity over the past 30 years due to their relative ease of implementation and computational performance. There have also been a number of attempts by the author to improve these methods [37–39].

The proposed new version of the velocity correction method can be considered to be a variation of the projection scheme originally proposed by Huser and Biringen [12]. In the first step of this scheme for the solution of the Helmholtz equation, temporal discretization is carried out with the Crank-Nicolson scheme on the viscous terms and the Adams-Bashforth method on the convective terms. Accordingly, the procedure is second-order-accurate in both time and space.

Velocity correction schemes involve two stages. In the first stage of the modified method, during the intermediate time step from t^n to $\tilde{t}$, the simplified Navier-Stokes equations (2) are solved, *i.e.*:

$$\begin{aligned}\frac{\partial \tilde{u}}{\partial t}+\frac{\partial \tilde{u}^2}{\partial x}+\frac{\partial}{\partial y}\big(\tilde{u}\tilde{v}\big)&=-\frac{\partial \tilde{p}^n}{\partial x}+\frac{1}{\mathrm{Re}}\,\vec{\nabla}^2\tilde{u},\\ \frac{\partial \tilde{v}}{\partial t}+\frac{\partial}{\partial x}\big(\tilde{u}\tilde{v}\big)+\frac{\partial \tilde{v}^2}{\partial y}&=-\frac{\partial \tilde{p}^n}{\partial y}+\frac{1}{\mathrm{Re}}\,\vec{\nabla}^2\tilde{v},\end{aligned} \tag{3}$$

where $\tilde{u}=\tilde{u}(x,\,y,\,t)$, $\tilde{v}=\tilde{v}(x,\,y,\,t)$ are the intermediate velocity components and $\tilde{p}^n=\tilde{p}(x,\,y,\,t^n)$ is a known computational pressure.

Let u^n, $\tilde{u}^n$, v^n and $\tilde{v}^n$ denote discrete approximations to u, $\tilde{u}$, v and $\tilde{v}$, so that:

$$\begin{aligned}u^n&=u\big(x,\,y,\,t^n\big),\quad \tilde{u}^n=\tilde{u}\big(x,\,y,\,t^n\big),\\ v^n&=v\big(x,\,y,\,t^n\big),\quad \tilde{v}^n=\tilde{v}\big(x,\,y,\,t^n\big).\end{aligned} \tag{4}$$

Equations (3) are to be solved subject to the initial and boundary conditions taken from the assumption that, on the $\partial\Omega$ boundaries and at the time level $t=t^n$, the intermediate velocity components $\tilde{u}$, $\tilde{v}$ are equal to the physical velocity components u, v:

$$\begin{aligned}\tilde{u}\Big|_{\partial\Omega}&=u\Big|_{\partial\Omega},\quad \tilde{v}\Big|_{\partial\Omega}=v\Big|_{\partial\Omega},\\ \tilde{u}^n&=u^n,\quad \tilde{v}^n=v^n.\end{aligned} \tag{5}$$

In the second stage, at every time step $\Delta t=t_{n+1}-t_n$ for the time step from $\tilde{t}$ to t^{n+1}, we solve the following equations:

$$\begin{aligned}u^{n+1}&=\tilde{u}-\frac{\Delta t}{2}\left(\frac{\partial \tilde{p}^{n+1}}{\partial x}-\frac{\partial \tilde{p}^n}{\partial x}\right),\\ v^{n+1}&=\tilde{v}-\frac{\Delta t}{2}\left(\frac{\partial \tilde{p}^{n+1}}{\partial y}-\frac{\partial \tilde{p}^n}{\partial y}\right),\end{aligned} \tag{6}$$

obtained after integration of the equations coupling the velocity fields with the derivatives of computational pressure:

$$\begin{aligned}\frac{\partial u}{\partial t}&=\frac{\partial \tilde{u}}{\partial t}-\frac{1}{2}\left(\frac{\partial \tilde{p}^{n+1}}{\partial x}-\frac{\partial \tilde{p}^n}{\partial x}\right),\\ \frac{\partial v}{\partial t}&=\frac{\partial \tilde{v}}{\partial t}-\frac{1}{2}\left(\frac{\partial \tilde{p}^{n+1}}{\partial y}-\frac{\partial \tilde{p}^n}{\partial y}\right).\end{aligned} \tag{7}$$

By differentiating Equations (6) with respect to x and y, respectively, adding the resulting equations and making use of Equation (1), we can obtain the Poisson equation for the computational pressure $\tilde{p}$ at the time level t^{n+1}:

$$\vec{\nabla}^2\tilde{p}^{n+1}=\vec{\nabla}^2\tilde{p}^n+\frac{2}{\Delta t}\left(\frac{\partial \tilde{u}}{\partial x}+\frac{\partial \tilde{v}}{\partial y}\right), \tag{8}$$

subject to the Neumann boundary conditions:

$$\left.\frac{\partial \tilde{p}^{n+1}}{\partial \vec{n}}\right|_{\partial\Omega}=0, \tag{9}$$

at all boundaries (resulting from relationships (6) provided that $\partial\tilde{p}/\partial\vec{n}$ vanishes at the first time step), where $\vec{n}$ is a vector normal to the boundaries.

Equation (9) is an artificial Neumann boundary condition not satisfied by the exact pressure. This boundary condition will induce a numerical (spurious) boundary layer [30], which will in turn result in a loss of accuracy (*e.g.* the calculated computational pressure in [12] is a second-order approximation to the true pressure).

3. Transformation of the domain of solution

The considered domain of solution (Figure 1) is transformed into a simply connected rectangle. The transformation is based on the theory of complex functions [40, 41] and consists of two consecutive steps.

First, the exterior of the rotated NACA 0012 profile in the complex plane

$$z = x + iy \tag{10}$$

is transformed into the exterior of a circle in the complex plane

$$\lambda = \mu + i\nu \tag{11}$$

by using the mapping function assumed in the form of a series of rational fractions,

$$z = \lambda + \sum_{n=1}^{N} c_n \left(\frac{a}{\lambda - \lambda_0} \right)^n, \tag{12}$$

wherein the symbols denote: c_n $(n = 1, 2, \ldots, N)$ - complex coefficients, a, λ_0 – the radius and the centre of the circle.

Next, a corresponding flow of ideal fluid is generated by a vortex located in the centre of the disc. The second mapping function is thus represented by the formula:

$$w(\lambda) = -i \ln \frac{\lambda - \lambda_0}{a}, \tag{13}$$

where i is the imaginary unit. Consequently, the complex potential (13)

$$w = \xi + i\eta \tag{14}$$

transforms the original domain into a rectangle (Figure 2). The upper AB side of this rectangle corresponds to the whole NACA 0012 profile, the lower CD side corresponds to the outer boundary, the two remaining segments, AC and BD, represent the same auxiliary cut in the z-plane, Equation (10), while the ε angle determines the image of the trailing edge of the aerofoil on the circle.

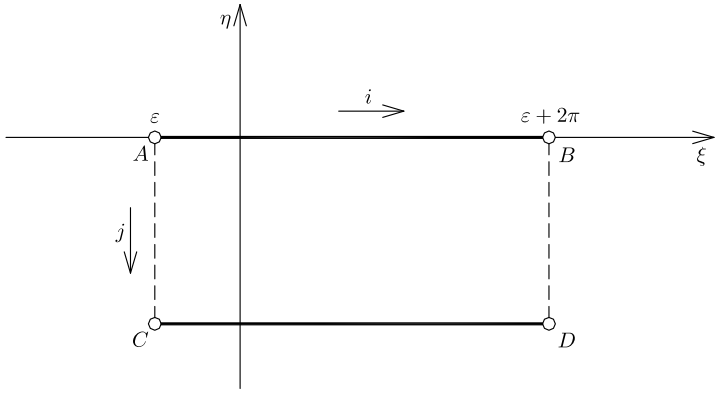

Figure 2. Canonical domain in the $\xi \times \eta$ plane

The substitution of the equation of circle written in polar co-ordinates r, ϑ in the λ plane, Equation (11):

$$\lambda = \lambda_0 + r e^{i\vartheta}, \tag{15}$$

into Equation (13) yields equations of family lines in the w plane, Equation (14):

$$\begin{aligned} \xi &= \vartheta, \;\; \vartheta \in [0, 2\pi], \\ \eta &= -\ln \frac{r}{a}, \;\; r \in [a, r_{\max}]. \end{aligned} \tag{16}$$

Thus a rectangular grid, $N_\xi \times N_\eta$, in the w plane:

$$\begin{aligned} \xi &= \varepsilon + i\Delta\xi, \;\; \Delta\xi = 2\pi/N_\xi, \;\; (i = 0,1,\ldots,N_\xi), \\ \eta &= j\Delta\eta, \;\; \Delta\eta = -\frac{1}{N_\eta} \ln \frac{r_{\max}}{a}, \;\; (j = 0,1,\ldots,N_\eta), \end{aligned} \tag{17}$$

is transformed into an orthogonal and conformal O-type grid in the z plane, Equation (10). An example of this kind of grid is shown in Figure 3 (some knots in the inner sub-domain are omitted for the sake of clarity).

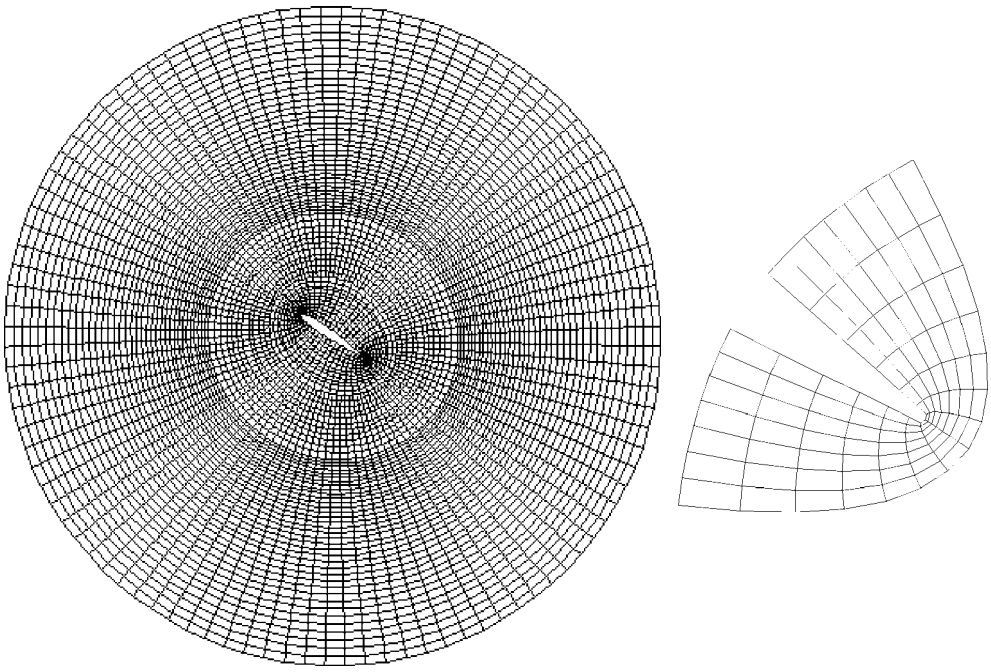

Figure 3. A computational O-type grid in the whole domain and in the neighbourhood of the trailing edge grid, generated for parameters: $r_{\max} = 15a$, $N_\xi = 100$, $N_\eta = 100$

The transformation of the physical domain (Figure 1) into the canonical one shown in Figure 2 is equivalent to the change of independent variables (x, y) to (ξ, η) in the considered partial differential problem.

The necessary expressions for the derivatives in the canonical domain are as follows (mapping functions (12) and (13) satisfy the Cauchy-Riemann conditions):

$$\begin{aligned}\frac{\partial}{\partial x} &= A\frac{\partial}{\partial \xi} + B\frac{\partial}{\partial \eta},\\ \frac{\partial}{\partial y} &= -B\frac{\partial}{\partial \xi} + A\frac{\partial}{\partial \eta},\\ \Delta_{xy} &= \alpha \Delta_{\xi\eta},\end{aligned} \tag{18}$$

where

$$A = \mu_x \xi_\mu - \nu_x \eta_\mu, \quad B = \mu_x \eta_\mu + \nu_x \xi_\mu,$$

$$\alpha = \left|\left(\frac{\mathrm{d}z}{\mathrm{d}\lambda}\right)^{-1}\right|^2 \left|\frac{\mathrm{d}w}{\mathrm{d}\lambda}\right|^2,$$

$$\mu_x + i\nu_x = \frac{\mathrm{d}\lambda}{\mathrm{d}z} = \left(\frac{\mathrm{d}z}{\mathrm{d}\lambda}\right)^{-1}, \quad \xi_\mu + i\eta_\mu = \frac{\mathrm{d}w}{\mathrm{d}\lambda} = -i\frac{1}{\lambda - \lambda_0}.$$

It is worth mentioning that the accuracy of the transformation can be controlled due to the analytically-numerical form of function (12) and that derivatives of the mapping functions can be calculated exactly, without any computational errors.

4. The numerical approach and results

The solution algorithm for each the time step can be written as follows.

1. Solve the initial-boundary value problem (3)–(5) for the $\tilde{u}$ and $\tilde{v}$ velocity components. The method of lines is adopted for this purpose, and compact finite differences schemes [42] of sixth-order accuracy are used to approximate derivatives with respect to spatial independent variables. Thus the following system of ordinary differential equations can be arrived at in all the internal k, l nodes of an assumed computational grid (17):

$$\begin{aligned}\frac{\mathrm{d}\tilde{u}_{k,l}}{\mathrm{d}t} &= F_1(\tilde{u}_{i,j}, \tilde{v}_{i,j}),\\ \frac{\mathrm{d}\tilde{v}_{k,l}}{\mathrm{d}t} &= F_2(\tilde{u}_{i,j}, \tilde{v}_{i,j}),\end{aligned} \tag{19}$$

where the right-hand sides $F_1(\tilde{u}_{i,j}, \tilde{v}_{i,j})$ and $F_2(\tilde{u}_{i,j}, \tilde{v}_{i,j})$ are spatially discretized Equations (3) and (5) and indices i, j are identical with mesh points (17).

The initial value problem obtained in this way can be integrated by applying the standard low-memory third-order Runge-Kutta method (Heun's method) [43, 44]. The preliminary numerical experiments conclusively demonstrate that integration over the $\tilde{t} - t^n = \Delta t/2$ half time step yields the best results and satisfactory numerical stability, compared with other integration time steps.

2. Solve Equation (8) for computational pressure $\tilde{p}^{n+1}$ with the homogeneous boundary conditions (9). The fourth-order accurate approximation to the Poisson equation (8) requires additional numerical boundary conditions, the choice of which is crucial for the creation of a stable and accurate scheme. An unsteady equation is therefore considered instead of Equation (8) in the steady form:

$$\frac{\partial \tilde{p}^{n+1}}{\partial \tau} = \vec{\nabla}^2 \tilde{p}^{n+1} - \vec{\nabla}^2 \tilde{p}^n - \frac{2}{\Delta t}\left(\frac{\partial \tilde{u}}{\partial x} + \frac{\partial \tilde{v}}{\partial y}\right), \tag{20}$$

where the time-like independent variable τ tends to infinity when the steady state is achieved. In order to obtain numerical solutions of high accuracy, in the process of

advancing from the initial condition $\tilde{p}^{n+1}\big|_{\tau=0} = \tilde{p}^n$ to the steady state, a modified five-level Runge-Kutta integration scheme is employed [45, 46]. The spatial derivatives and the boundary conditions are discretized by means of sixth-order tridiagonal approximations [42] together with finite-difference schemes having a truncation error of fourth-order accuracy [44].

3. Update physical velocity components u^{n+1}, v^{n+1} using Equations (6).

The initial and outer boundary conditions chosen for computation are the solution of irrotational flow of inviscid and incompressible fluid. The well-known complex potential describing this flow in a circular domain has the following form [2]:

$$W(\lambda) = V_\infty(\lambda - \lambda_0) + \frac{\Gamma}{2\pi i}\ln(\lambda - \lambda_0) + \frac{V_\infty a^2}{\lambda - \lambda_0}, \tag{21}$$

in which V_∞ denotes a free-stream velocity in infinity and the value of vortex circulation:

$$\Gamma = 4\pi a V_\infty \sin\varepsilon, \tag{22}$$

is taken from Joukowski's condition. The correspondence of the complex potential $W(\lambda)$ to the original z plane, Equation (10), stems directly from the mapping function (12), *i.e.* $\lambda = \lambda(z)$.

For easier comparison of numerical results with those presented in the literature, a stream-function field has been computed as a solution of the Poisson equation:

$$\frac{\partial^2\psi}{\partial\xi^2} + \frac{\partial^2\psi}{\partial\eta^2} = -\frac{\omega}{\alpha}, \tag{23}$$

for a known distribution of vorticity, $\omega = \partial v/\partial x - \partial u/\partial y$, with boundary conditions:

$$\begin{aligned} \psi\Big|_{\eta=0} &= \psi_{\text{inv.}}\Big|_{\eta=0}, \\ \frac{\partial\psi}{\partial\eta}\bigg|_{\eta=N_\eta} &= \frac{1}{\alpha}\left(A v_{\text{inv.}} - B u_{\text{inv.}}\right)\bigg|_{\eta=N_\eta}. \end{aligned} \tag{24}$$

Calculations on the 100×100 grid (Figure 3) were made with the following values of input data:

- time steps: $\Delta t = 1\cdot 10^{-4}$, $\mathrm{Re} = 400$; $\Delta t = 1\cdot 10^{-3}$, $\mathrm{Re} \geq 600$;
- pseudo-time step: $\Delta\tau = 1\cdot 10^{-4}$;
- accuracy of the steady state solution of the system (19): $1\cdot 10^{-10} \leq \varepsilon_1 \leq 1\cdot 10^{-8}$ ($\mathrm{Re} = 400$, 600);
- accuracy of the steady state solution of Equation (20): $\varepsilon_2 = 1\cdot 10^{-6}$.

The computations started for $\mathrm{Re} = 400$ with the initial conditions assumed as the potential flow solution. A steady state was reached in nearly 5000 iterations, yielding the stream-function contours and velocity vectors which can be seen in Figures 4 and 5. It turned out that the solution for $\mathrm{Re} = 600$ with initial conditions taken as the flow field for $\mathrm{Re} = 400$ was also stable, and in this case 800 iterations were necessary to converge the procedure (Figures 6 and 7).

Calculations for higher Reynolds numbers indicated that simulated flows became unsteady and unstable. To illustrate the present method the unsteady flow around the NACA 0012 aerofoil at the Reynolds number of 10^3 was computed, with the start-up flow conditions set as the flow field for $\mathrm{Re} = 600$. The reason for this

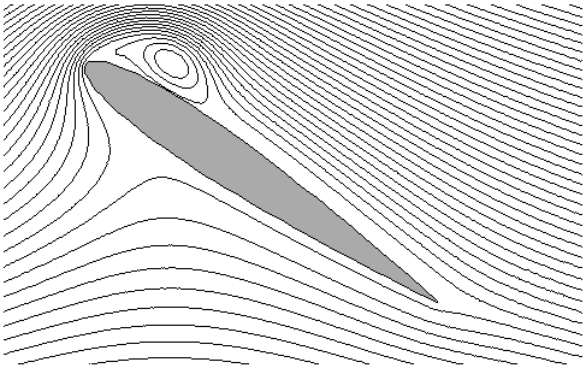

Figure 4. Stream-function contours for $Re = 400$ on the 100×100 grid

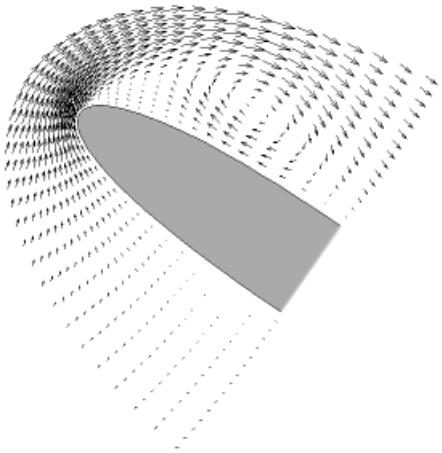

Figure 5. Velocity vectors for $Re = 400$ on the 100×100 grid in the region near the profile

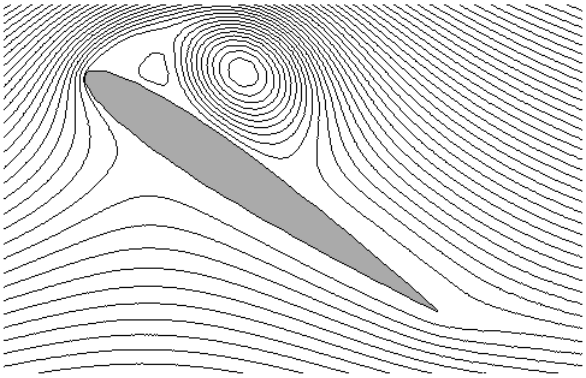

Figure 6. Stream-function contours for $\mathrm{Re} = 600$ on the 100×100 grid

choice was that there existed numerous numerical results and experimental visualizations of this case in the literature [47–50], necessary for comparison. Unsteady flows for $\mathrm{Re} > 1000$ were also studied by a few researches [47, 51, 52].

Figures 8–12 show the flow structure in five non-dimensionalized moments of time with isolines for equidistant stream-function increments (not all of the small

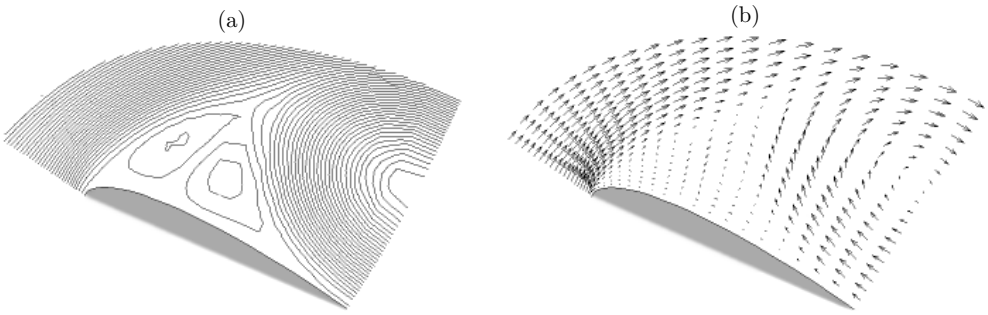

Figure 7. (a) Stream-function contours and (b) velocity vectors for $\mathrm{Re} = 600$ on the 100×100 grid in the region near the profile

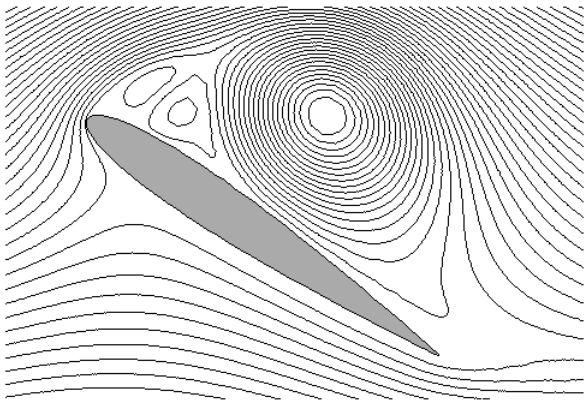

Figure 8. Stream-function contours for $\mathrm{Re} = 1000$ on the 100×100 grid at $t = 1$

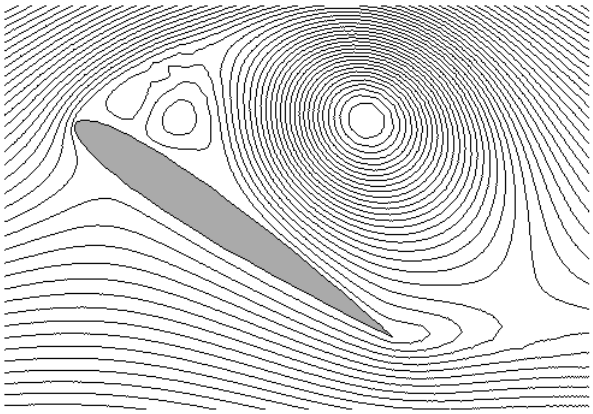

Figure 9. Stream-function contours for $\mathrm{Re} = 1000$ on the 100×100 grid at $t = 2$

vortices are shown). The time evolution of the flow field is correctly reproduced taking into account the results reported in [47], which unfortunately display the flow field in the neighbourhood of the profile only. All captured main and secondary vortices are similar to those detected by experimental observations and numerical simulations. Increasing the number of time steps leads to numerical instabilities and spurious results.

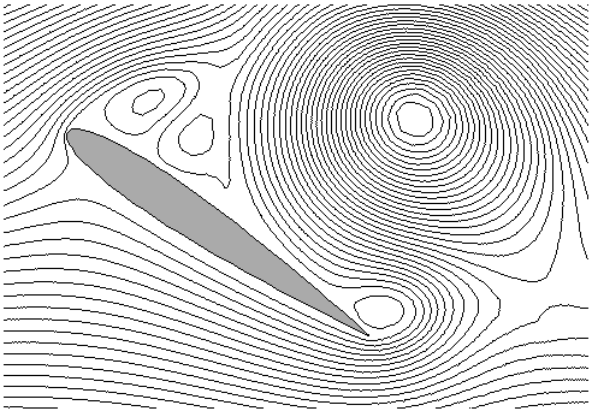

Figure 10. Stream-function contours for $\mathrm{Re} = 1000$ on the 100×100 grid at $t = 3$

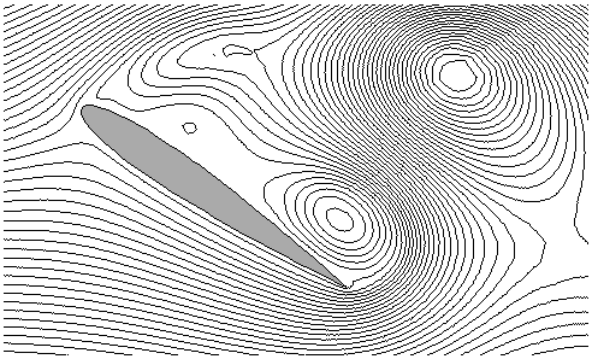

Figure 11. Stream-function contours for $\mathrm{Re} = 1000$ on the 100×100 grid at $t = 4$

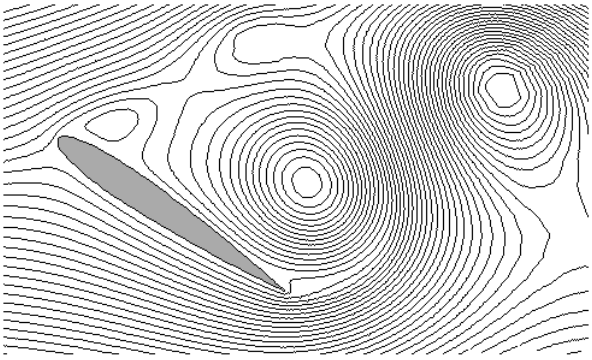

Figure 12. Stream-function contours for $\mathrm{Re} = 1000$ on the 100×100 grid at $t = 5.5$

The influence of the outflow boundary conditions was studied by investigating the effect of size of the computational domain. For this purpose a 100×200 computational grid with $r_{\max} = 30a$ (Equation (17)) was generated. Nearly 9000 iterations were done for $\mathrm{Re} = 400$ (a steady state solution, see Figures 13 and 14) and the initial data distributions given by the potential flow field with the time step of $\Delta t = 1 \cdot 10^{-4}$, while the remaining parameters of the calculation were the same as in the previous case of the 100×100 grid. Afterwards, a converged solution (2000 time steps) for the

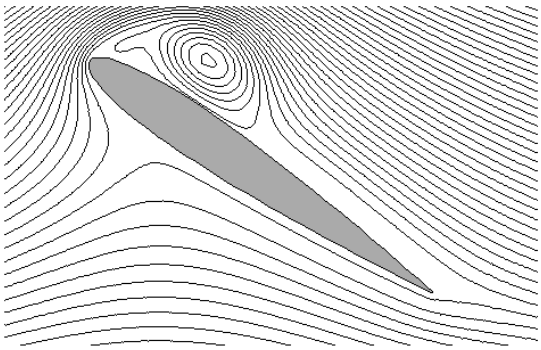

Figure 13. Stream-function contours for $\mathrm{Re} = 400$ on the 100×200 grid

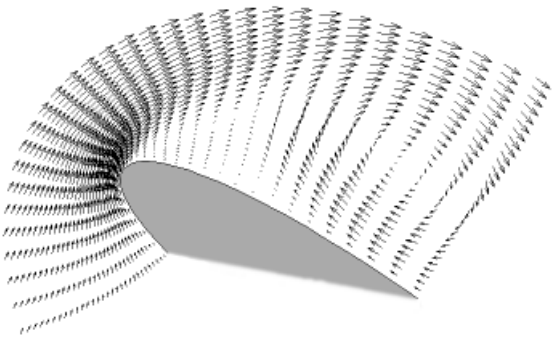

Figure 14. Velocity vectors for $\mathrm{Re} = 400$ on the 100×200 grid in the region near the profile

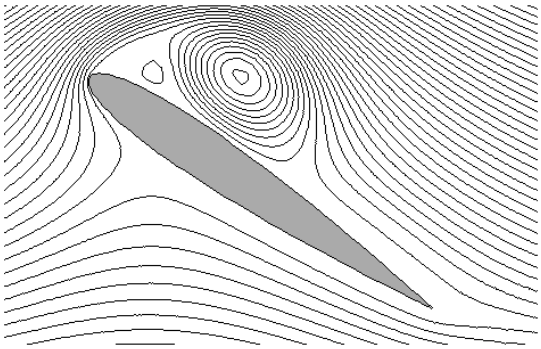

Figure 15. Stream-function contours for $\mathrm{Re} = 600$ on the 100×200 grid

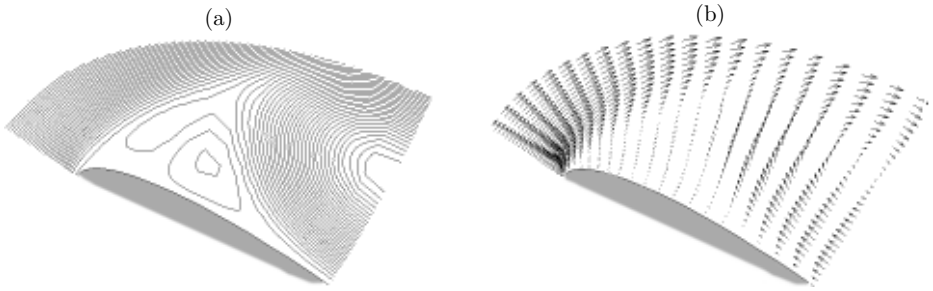

Figure 16. (a) Stream-function contours and (b) velocity vectors for $\mathrm{Re} = 600$ on the 100×200 grid in the region near the profile

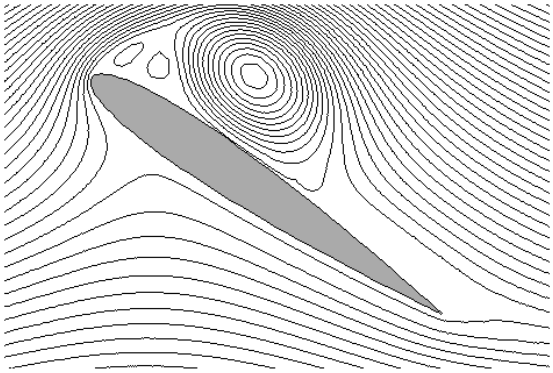

Figure 17. Stream-function contours for $Re = 1000$ on the 100×200 grid at $t = 0.5$

$\mathrm{Re} = 600$ was obtained with these initial conditions, $\Delta t = 2 \cdot 10^{-4}$ and $\varepsilon_1 = 1 \cdot 10^{-7}$, (Figures 15 and 16); the time step on the 100×200 grid was changed due to the stability criterion. The results for $\mathrm{Re} = 400$ (Figures 4, 5, 13 and 14) and $\mathrm{Re} = 600$ (Figures 6, 7, 15 and 16) on two different grids show a certain discrepancy in the images of the corresponding stream-function contours. It has been confirmed that the computation requires suitable variation and control of all input data.

The solution computed for $\mathrm{Re} = 400$ with $1 \cdot 10^{-4} \leq \Delta t \leq 5 \cdot 10^{-4}$ was subsequently used as the initial guess for the case of $\mathrm{Re} = 1000$; the results are plotted in Figures 17–26. Numerical simulations of vortex shedding on the larger 100×200 grid were continued for almost twice the time interval of the 100×100 grid.

5. Concluding remarks

A modified velocity correction method of simulation of two-dimensional unsteady external incompressible viscous flows has been presented in this paper. The method can be easily extended to three-dimensional non-stationary flows. New algorithms with fourth- and sixth-order accuracy in time and space for provisional velocity field have been developed. The proposed method seems to be promising considering the computational effort involved and the achieved agreement of numerical results with solutions reported in the literature. As expected, the re-circulation regions in-

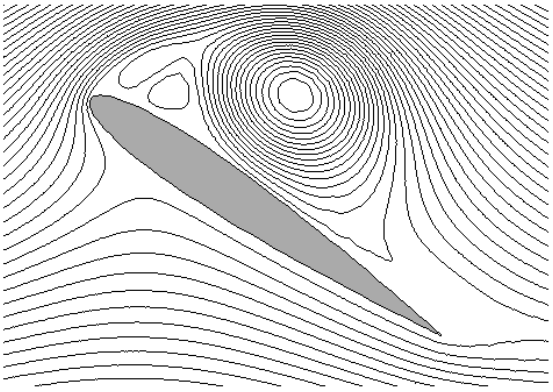

Figure 18. Stream-function contours for $\mathrm{Re} = 1000$ on the 100×200 grid at $t = 1$

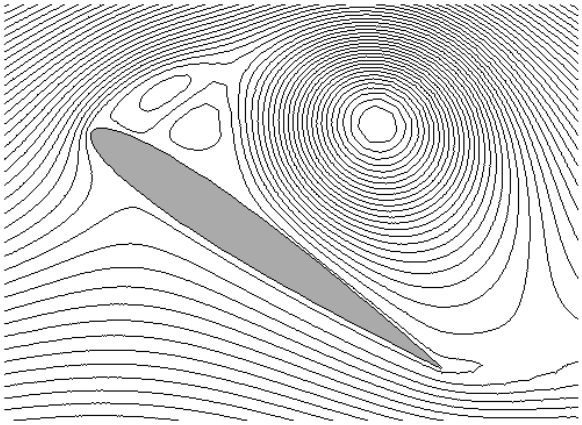

Figure 19. Stream-function contours for $\mathrm{Re} = 1000$ on the 100×200 grid at $t = 2$

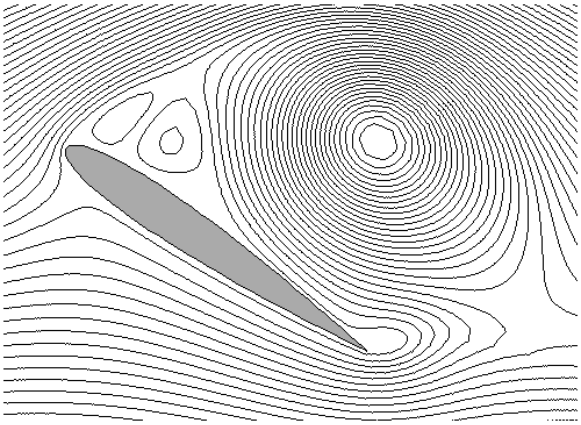

Figure 20. Stream-function contours for $\mathrm{Re} = 1000$ on the 100×200 grid at $t = 3$

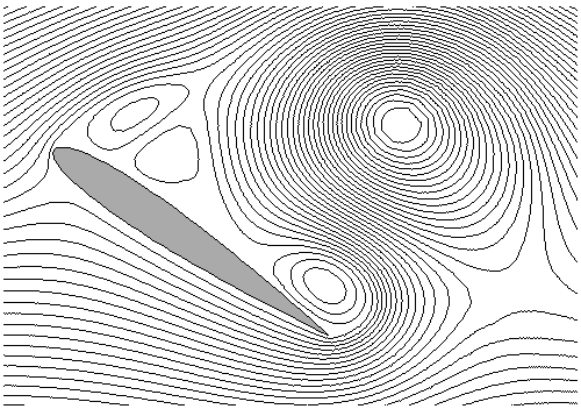

Figure 21. Stream-function contours for $\mathrm{Re} = 1000$ on the 100×200 grid at $t = 4$

crease in size with time until the system becomes unstable and vortices vanish in an oscillatory manner. It should be recalled that the imposed velocity components at the outer boundary, obtained from the potential flow solution, tend to uniform

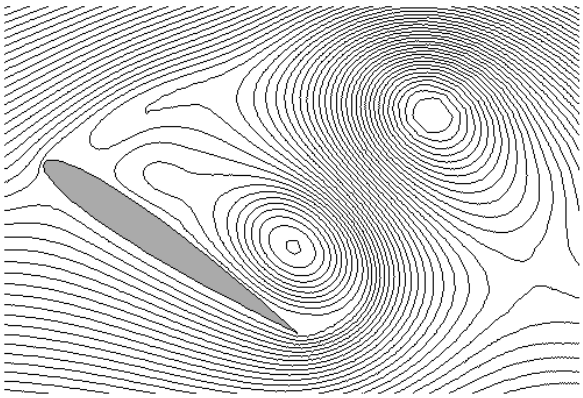

Figure 22. Stream-function contours for $\mathrm{Re} = 1000$ on the 100×200 grid at $t = 5$

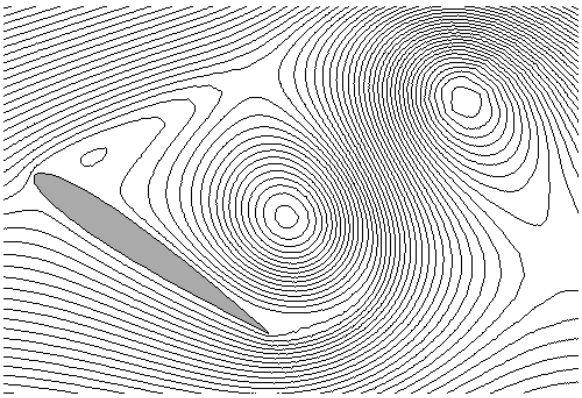

Figure 23. Stream-function contours for $\mathrm{Re} = 1000$ on the 100×200 grid at $t = 6$

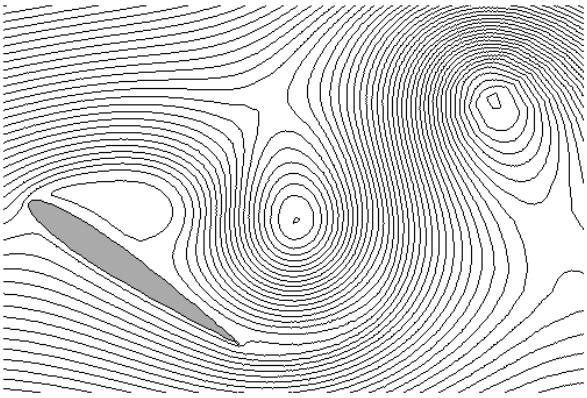

Figure 24. Stream-function contours for $\mathrm{Re} = 1000$ on the 100×200 grid at $t = 7$

incompressible flow $(u_{\mathrm{inv.}}, v_{\mathrm{inv.}}) \to (1, 0)$, while the size of the computational region increases. Besides, these boundary conditions can also be normalized, as has been confirmed by numerical experiments

The aim of future research will be detailed examination of the flow for higher Reynolds numbers. At the same time, some improvements need to be introduced to

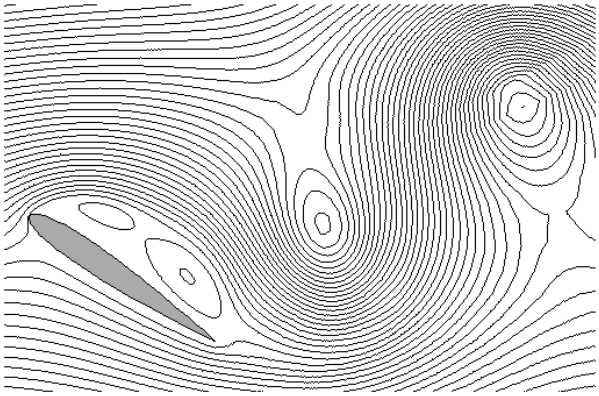

Figure 25. Stream-function contours for $\mathrm{Re} = 1000$ on the 100×200 grid at $t = 8$

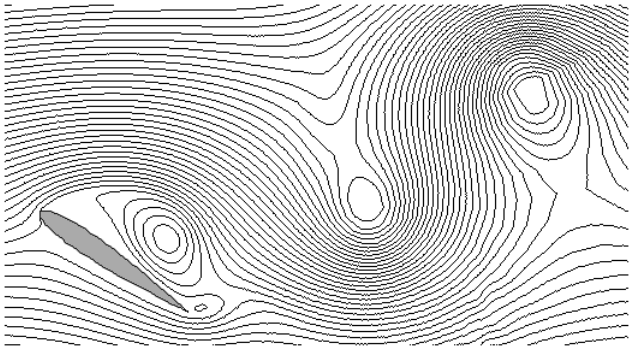

Figure 26. Stream-function contours for $\mathrm{Re} = 1000$ on the 100×200 grid at $t = 9.5$

increase the efficiency of the method. It is also necessary to consider other algorithms to solve the Poisson equation for computational pressure. Furthermore, a currently investigated aspect of this problem are attempts to establish the correct outflow boundary conditions required to generate a vortex sheet in the region outside the profile. Another important problem is the choice of a suitable computational grid. In order to compute the flow accurately in multiple regions of vortices, the grid distribution requires particular refinements. Producing two overlapping grids should be the most suitable: one in the neighbourhood of the profile, the other containing a region with a predicting vortex sheet.

References

[1] Prosnak W J and Kosma Z 1987 *Scientific Bulletin of Institute of Fluid-Flow Machinery of PAS*, Gdansk, Poland **240/1180/87** (in Polish)

[2] Batchelor G K 1990 *An Introduction to Fluid Dynamics*, Cambridge University Press

[3] Warsi Z U A 1993 *Fluid Dynamics: Theoretical and Computational Approaches*, CRC Press

[4] Roache P J 1998 *Computational Fluid Dynamics*, 2nd Edition, Albuquerque, Hermosa

[5] Chorin A J 1968 *Math. Comput.* **22** 745

[6] Kim J and Moin P 1985 *J. Comput. Phys.* **59** 308

[7] Hirsch Ch 1990 *Numerical Computational of Internal and External Flows*, Vol 2: *Computational Methods for Inviscid and Viscous Flows*, John Wiley & Sons, Chichester – New York

[8] Tanahashi T and Okanaga H 1990 *Int. J. Numer. Meth. Fluids* **11** 479

[9] Gresho P M 1990 *Int. J. Numer. Meth. Fluids* **11** 587

[10] Kovacs A and Kawahara M 1991 *Int. J. Numer. Meth. Fluids* **13** 403
[11] Karniadakis G M 1991 *J. Comput. Phys.* **97** 414
[12] Huser A D and Biringen S 1992 *Int. J. Numer. Meth. Fluids* **14** 1087
[13] Ren G and Utnes T 1993 *Int. J. Numer. Meth. Fluids* **17** 349
[14] Pinelli A and Vacca A 1994 *Int. J. Numer. Meth. Fluids* **18** 781
[15] Turek S 1996 *Int. J. Numer. Meth. Fluids* **22** 987
[16] Ferziger J H and Perić M 1996 *Computational Methods for Fluid Dynamics*, Springer-Verlag, Berlin – Heidelberg – New York
[17] Hugues S and Randriamampianina A 1998 *Int. J. Numer. Meth. Fluids* **28** 501
[18] Goldberg D and Ruas V 1999 *Int. J. Numer. Meth. Fluids* **30** 233
[19] Guo D X 2000 *Appl. Numer. Math.* **35** 307
[20] Boivin S, Cairé F and Hérard J-M 2000 *Int. J. Therm. Sci.* **39** 806
[21] Minev P D 2001 *Int. J. Numer. Meth. Fluids* **36** 441
[22] Brown D L, Cortez R and Minion M L 2001 *J. Comput. Phys.* **168** 464
[23] Liu C H and Leung D Y C 2001 *Comput. Meth. Appl. Mech. Engng.* **190** 4301
[24] Auteri F, Saleri F and Vigevano L 2001 *Comput. Meth. Appl. Mech. Engng.* **190** 6927
[25] Friedrich R, Hüttl T J, Manhart M and Wagner C 2001 *Comput. Fluids* **30** 555
[26] Christon M A 2002 *Int. J. Numer. Meth. Fluids* **38** 1177
[27] Auteri F and Parolini N 2002 *J. Comput. Phys.* **175** 1
[28] Stevens D E, Chan S T and Gresho P 2002 *Int. J. Numer. Meth. Fluids* **40** 1303
[29] Botella O 2002*Comput. Fluids* **31** 397
[30] Dagan A 2003 *Comput. Fluids* **32** 1213
[31] Guermond J L and Shen J 2003 *J. Comput. Phys.* **192** 262
[32] Grauer R and Spanier F 2003 *J. Comput. Phys.* **192** 727
[33] Manhart A 2004 *Comput. Fluids* **33** 435
[34] Fernandez-Feria R and Sanmiguel-Rojas E 2004 *Comput. Fluids* **33** 463
[35] Löhner R 2004 *J. Comput. Phys.* **195** 143
[36] Minion M L 2004 *Appl. Numer. Math.* **48** 369
[37] Kosma Z 1994 *Z. Angew. Math. Mech.* (ZAMM) **74** 6 570
[38] Kosma Z 1999 *Determination of Laminar Incompressible Flows*, Monography of the Radom University of Technology (in Polish)
[39] Kosma Z 2003 *Numerical Simulation of Viscous Fluid Motions*, Monography of the Radom University of Technology (in Polish)
[40] Kosma Z 1987 *Bull. Ac. Pol.: Tech.* **35** 41
[41] Kosma Z 1989 *Scientific Bulletin of Institute of Fluid-Flow Machinery of PAS*, Gdansk, Poland **289/1249/89** (in Polish)
[42] Lele S K 1992 *J. Comput. Phys.* **103** 16
[43] Hairer E, Norset S P and Wanner G 1987 *Solving Ordinary Differential Equations I: Nonstiff Problems*, Springer-Verlag, Berlin – Heidelberg – New York
[44] Kosma Z 1999 *Numerical Methods for Engineering Applications*, Radom University of Technology Publishing, Poland (in Polish)
[45] Jameson A, Schmidt W and Turkel E 1981 *AIAA Paper* **81** 1259
[46] Hirsch Ch 1988 *Numerical Computational of Internal and External Flows* Vol 1: *Fundamentals of Numerical Discretization*, John Wiley & Sons, Chichester – New York
[47] Shen W-Z and Loc T P 1995 *Int. J. Numer. Meth. Fluids* **20** 1111
[48] Chou M-H and Huang W 1996 *Int. J. Numer. Meth. Fluids* **23** 711
[49] Bhaskaran R and Rothmayer A P 1998 *Comput. Fluids* **27** 903
[50] Bertagnolio F and Daube O 1998 *Int. J. Numer. Meth. Fluids* **28** 917
[51] Nair M T and Sengupta T K 1998 *Int. J. Numer. Meth. Fluids* **28** 215
[52] Murthy P S, Holla V S and Kamath H 2000 *Comput. Meth. Appl. Mech. Engng.* **186** 85